Bulletin of the Seismological Society of America, Vol. 76, No. 3, pp. 649–674, June 1986

RUPTURE HISTORY OF THE 1984 MORGAN HILL, CALIFORNIA, EARTHQUAKE FROM THE INVERSION OF STRONG MOTION RECORDS

BY STEPHEN H. HARTZELL AND THOMAS H. HEATON

ABSTRACT

Near-source strong motion velocity records and teleseismic short-period P waveforms are modeled to obtain the spatial and temporal distribution of slip for the 1984 Morgan Hill earthquake. Both forward modeling and constrained, least-squares inversion techniques are used to interpret the strong motion velocity waveforms in the frequency range of approximately 0.2 to 2.0 Hz. These data support a nearly unilateral rupture to the southeast with a rupture propagation velocity of nine-tenths of the local S-wave velocity. The majority of the slip occurs over a fault length of 25 km and to a first approximation can be interpreted as two main source regions, each with an extent of about 5 km with their centers separated by about 12 km. However, each of the sources has detailed structure of its own, and a simple two-point-source model is not an accurate representation of the Morgan Hill earthquake. The second source occurs about 4.5 sec after the first and is approximately 3 times larger. The maximum dislocation on the fault plane is about 1 m. The total moment of the earthquake is estimated to be 2.1×10^{25} dyne-cm. The Morgan Hill earthquake offers convincing evidence for very inhomogeneous slip and stress distributions on shallow strike-slip faults.

INTRODUCTION

The Morgan Hill earthquake of 24 April 1984 (21:15:18.8 UTC) is a moderate-sized event (M_L 6.2 USGS) which occurred on the Calaveras fault approximately 17 km southeast of San Jose, California. The epicenter is located at 37°18.56'N, 121°40.68'W with a hypocentral depth of 8.5 km (Cockerham and Eaton, 1984). This earthquake produced a significant set of near-source strong motion records; 12 ground-level, mostly free-field stations with accelerations greater than 0.1 g were recorded within 40 km of the epicenter. One of these stations (Coyote Lake Dam) recorded a peak acceleration of 1.3 g and a peak velocity of 79 cm/sec on a horizontal component. Other records of the strong motion data set suggest that this earthquake consisted of two main sources, or alternatively, a single source which produced a prominent "starting phase" and "stopping phase." In this paper, the strong motion velocity records and teleseismic short-period P waveforms are modeled to determine the distribution of coseismic slip. This slip distribution is then used to determine which of the above source models is correct, as well as, increase our general understanding of the build-up and release of stress on shallow strike-slip faults. Recent seismicity along this section of the Calaveras fault is discussed by Bakun (1980). Larger recent events are the 6 August 1979 Coyote Lake earthquake (M_L 5.9), located just south of the Morgan Hill rupture, the 29 August 1978 Halls Valley earthquakes (M_L 4.2 and M_L 3.9), and the 8 May 1979 Halls Valley earthquake (M_L 4.5).

DATA

The near-source strong motion velocity records are shown in Figure 1, a to c (Shakal *et al.*, 1984; Brady *et al.*, 1984). Unfortunately, most of the stations are not naturally rotated with respect to the fault orientation, with the majority of stations

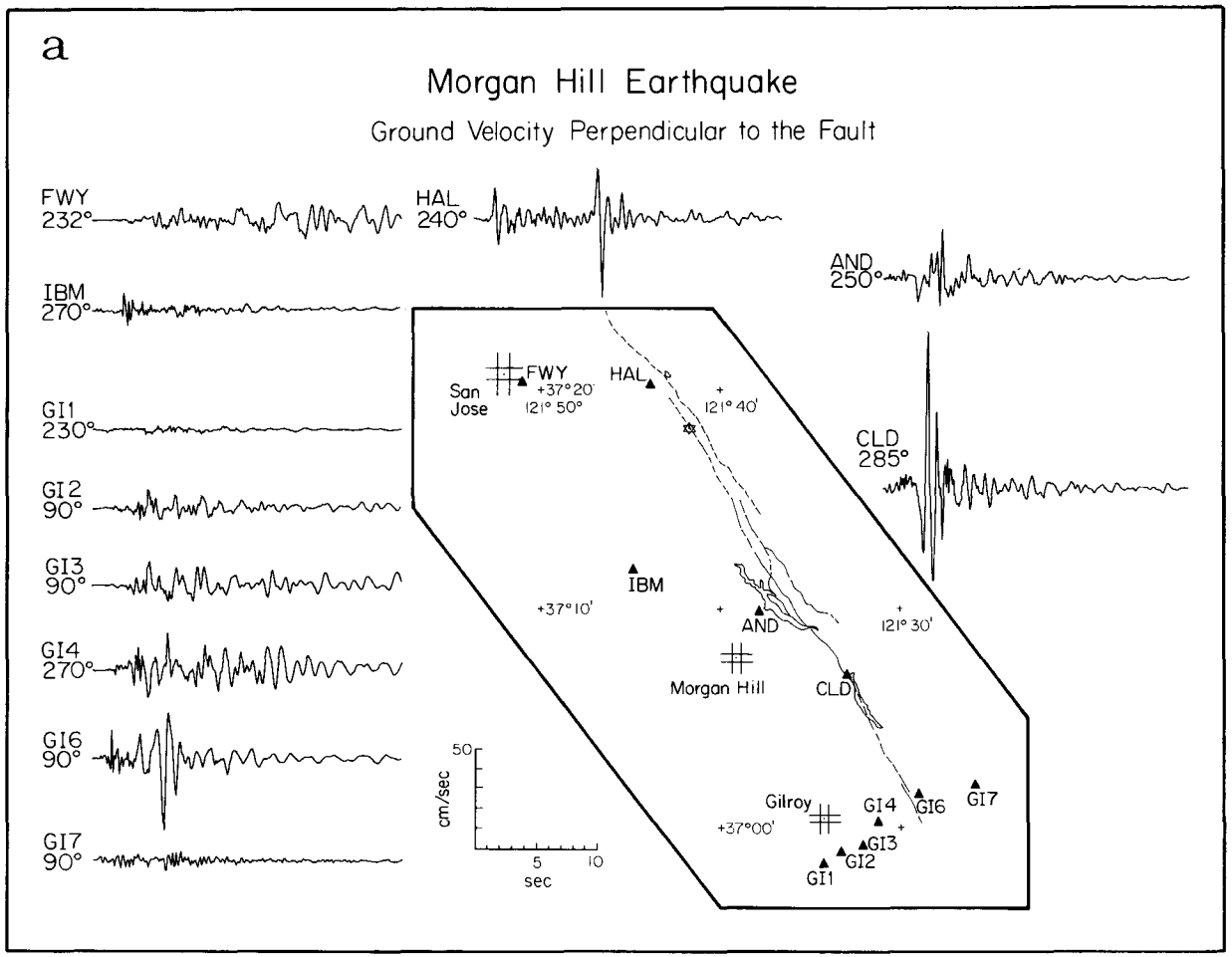

FIG. 1a. Strong motion velocity components perpendicular to the Calaveras fault zone.

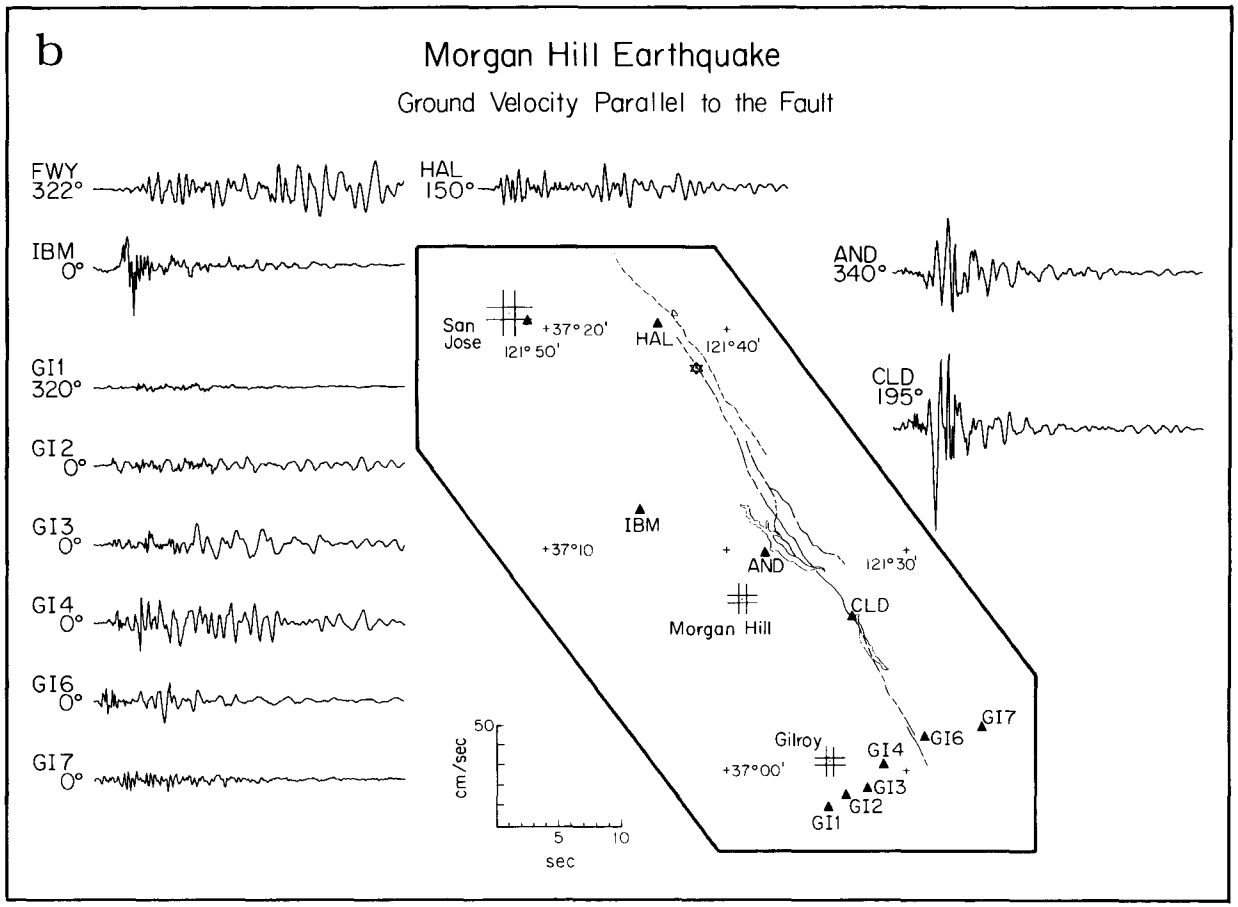

FIG. 1b. Strong motion velocity components parallel to the Calaveras fault zone.

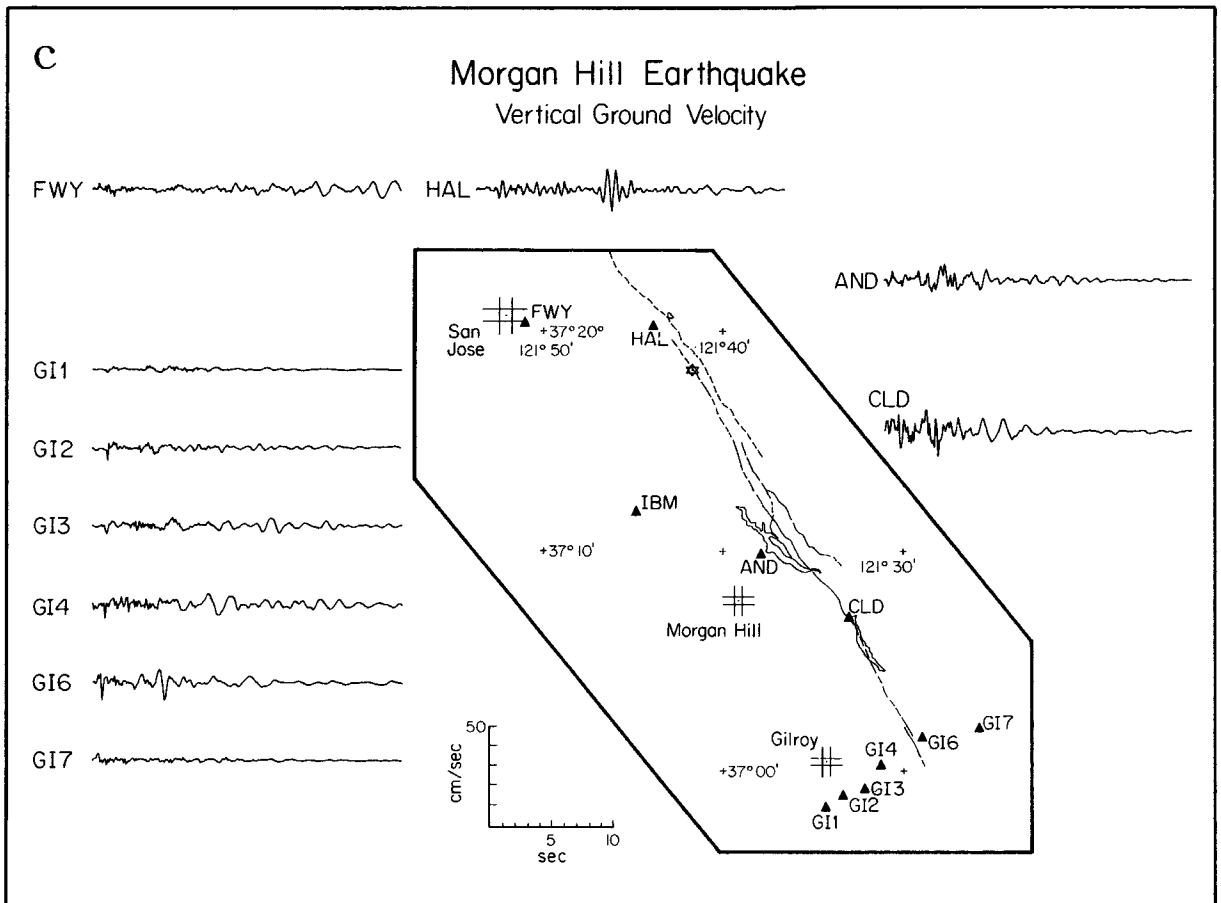

FIG. 1c. Vertical strong motion velocity components.

having orientations of about 30° from the fault strike (CLD is close to 45°). The traces are arranged such that Figure 1a contains the components of ground motion that are more nearly perpendicular to the fault strike. The components of fault motion that are more nearly parallel to the fault are in Figure 1b, and the vertical components are in Figure 1c. All of the records in these three figures are plotted using the same horizontal and vertical scales to facilitate comparisons. Table 1 lists the station names and their locations. The Calaveras fault zone is indicated in Figure 1 (a to c) by the southeast-trending dashed and solid lines. An estimate of the epicenter is given by the star. The location of the epicenter will be discussed further in the following section dealing with the fault model.

For a shallow, strike-slip source on the Calaveras fault, the perpendicular components in Figure 1a should be dominated by *SH*-type motion and, in general, these components are the largest. The Coyote Lake Dam station, which is located nearly on-strike with the mapped surface trace of the Calaveras fault and near the southern

TABLE 1

STRONG MOTION STATIONS

Station Code	Station Name	Data Source	Latitude (°)	Longitude (°)	Station Name (Switzer *et al.*, 1981)
HAL	Halls Valley	CDMG	37.338	121.731	HVR
CLD	Coyote Lake Dam	CDMG	37.117	121.550	CYD
AND	Anderson Dam (downstream)	USGS	37.165	121.631	ANL
FWY	San Jose 101/280/680 Freeways	USGS	37.340	121.851	SJH
IBM	IBM Santa Teresa Facility	IBM	37.197	121.747	—
GI1	Gilroy array 1	CDMG	36.973	121.572	G01
GI2	Gilroy array 2	CDMG	36.982	121.556	G02
GI3	Gilroy array 3	CDMG	36.987	121.536	G03
GI4	Gilroy array 4	CDMG	37.005	121.521	G04
GI6	Gilroy array 6	CDMG	37.026	121.483	G06
GI7	Gilroy array 7	CDMG	37.033	121.430	G07

end of the aftershock distribution, recorded a very large *S*-wave pulse, having a peak velocity of 79 cm/sec on the 285° component. The aftershocks extend a distance of 30 km from Halls Valley in the north to the northern end of Coyote Lake in the south (Cockerham and Eaton, 1984). In addition, since the epicenter is near the northern end of the aftershock pattern, initial analysis suggests that the large amplitudes at Coyote Lake Dam are due to the combined effects of its location near an *SH* radiation pattern maximum and directivity from southward propagation of the rupture. Niazi (1984) noted larger peak ground accelerations to the southeast of the source and related this observation to a southeast-propagating rupture with an average velocity of 0.7β.

Besides the Coyote Lake Dam site, stations that recorded large *SH* amplitudes are Halls Valley and stations in the Gilroy array (Figure 1a). There is a regular increase in the amplitude of the ground motion moving from Gilroy array station 1 toward the Calaveras fault to array station 6. Table 2 examines this increase. The values for station azimuth and radiation pattern in Table 2 assume a vertical strike-slip source at Anderson Reservoir, with a strike direction in line with Gilroy array station 6. The observed peak velocities are normalized to an amplitude of 1.0 for station 6. These amplitudes are not explained by a simple $\cos(2\theta)$ *SH* radiation pattern. Neither are they explained by the addition of a directivity term for a

southward-propagating rupture with a velocity of nine-tenths the shear wave velocity. These observations suggest there is amplification at station 6, perhaps by as much as a factor of 2. Although the crudely estimated amplitude pattern in Table 2 is within a factor of 2 of the observations for stations 2, 3, 4, and 6, the amplitude at station 7 is 5 times smaller than expected. For a vertical strike-slip fault in a half-space, the amplitude at station 7 should be similar to that at station 4. However, station 7 is much smaller. Structural complexities in the fault zone may be responsible for a shadowing effect at station 7. This argument ignores the possible amplification effects at station 4 by the Santa Clara Valley alluvium; however, station 7 is also located on sediments. To the north, Halls Valley is another station for which amplitudes are too large to be consistent with other data (supporting evidence given in the section on modeling results). Ground motions at this station, as well as at other stations located in the fault zone, may be amplified by a wave guide effect caused by lower velocities along the fault (Fend and McEvilly, 1983; Cormier and Spudich, 1984).

In addition to the above complexities, the San Jose freeway junction station and Gilroy array stations 2, 3, and 4 all have longer, more complex waveforms than

TABLE 2

PEAK VELOCITIES ACROSS GILROY ARRAY

Station	Azimuth (θ)	Observed Amplitude (cm/sec)	Normalized Observed Amplitude	*SH* Radiation Pattern ($\cos 2\theta$)	Normalized* Directivity Function ($V_R = 0.9\beta$)	Normalized Theoretical Amplitude
GI7	11.5	5.0	0.14	0.92	0.85	0.78
GI6	0.0	35.0	1.0	1.0	1.0	1.0
GI4	11.5	18.0	0.51	0.92	0.85	0.78
GI3	16.5	11.0	0.31	0.84	0.73	0.61
GI2	21.0	9.0	0.26	0.74	0.63	0.46
GI1	25.5	2.0	0.06	0.63	0.53	0.33

* $\dfrac{V_R}{\beta - V_R \cos\theta}$.

other stations at comparable source distances. This observation is most likely due to the fact that these stations are located on the thick sediments of the Santa Clara Valley. The IBM facility is located at the western edge of the valley and recorded a simpler waveform. Thus, there are several aspects of the Morgan Hill strong motion data set that suggest lateral heterogeneities in velocity structure have first-order effects on the strong ground motion waveforms and amplitudes at certain stations.

Another factor which makes the Morgan Hill strong motion records difficult to model is the relatively high-frequency nature of the motions. Figure 2 compares two horizontal components of ground velocity: the 285° component from the Coyote Lake Dam station for the 1984 Morgan Hill earthquake (M_L 6.2), and the 230° component from the El Centro array station 7 for the 1979 Imperial Valley earthquake (M_L 6.6). Both of these records are mainly *SH* motion and were recorded at similar positions with respect to the traces of the Calaveras and Imperial faults. Both stations also lie in the direction of rupture propagation. The Morgan Hill record is significantly higher frequency (~1.25 Hz). High-frequency data make forward modeling difficult and also complicate formal inversion procedures, requiring more accurate timing to correctly fit individual phases. The higher frequency Morgan Hill records imply a source with rapid spatial changes in dislocation amplitudes, or alternatively a complex rupture propagation.

Prior to modeling, the velocity records are processed. The velocity records are obtained by integrating the instrument-corrected accelerograms. The velocity waveforms are first bandpass-filtered from 0.2 to 5.0 Hz using a zero-phase-shift Butterworth filter (Oppenheim and Schafer, 1975). The filtering is done to remove frequencies outside the bandwidth for which Green's functions could be conveniently calculated. This bandwidth includes most of the predominant frequencies in the velocity records (1.0 to 2.0 Hz) so that the filtered and unfiltered waveforms are

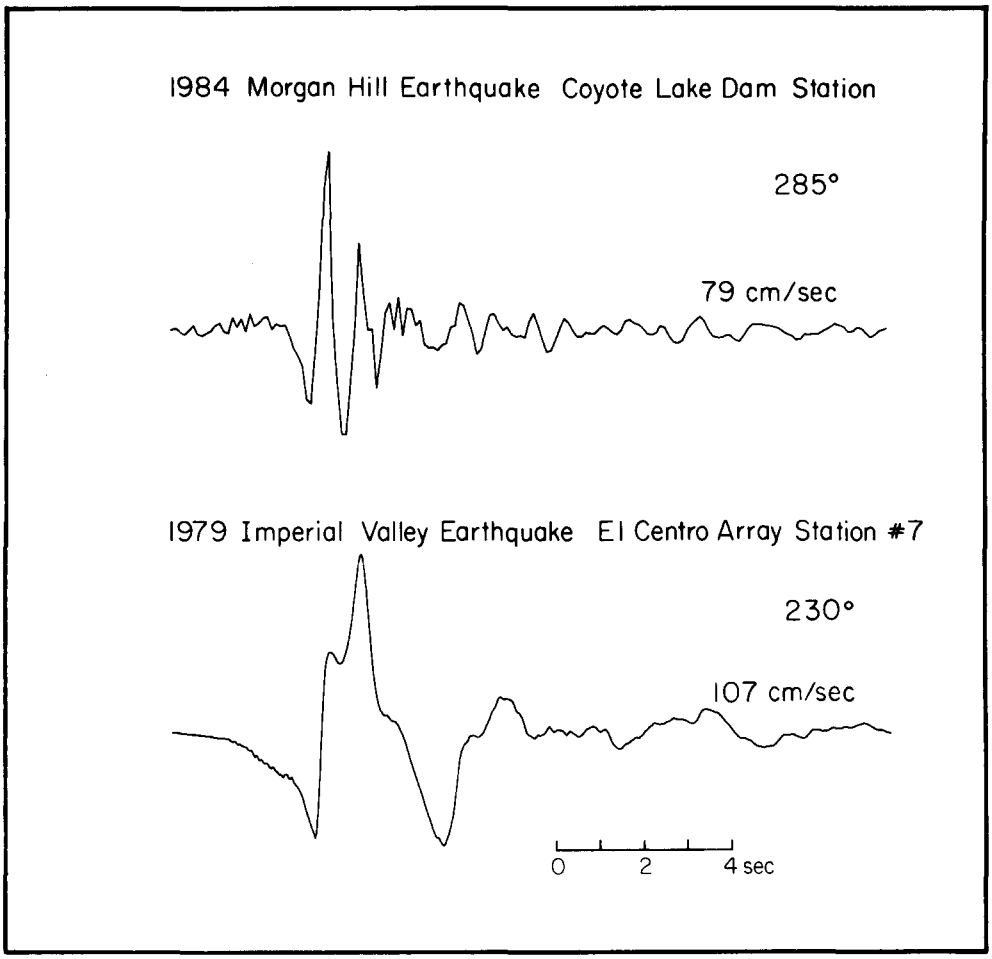

FIG. 2. Comparison of local, transverse velocity records (*SH* waveforms) for the 1984 Morgan Hill and the 1979 Imperial Valley earthquakes.

very similar in amplitude and shape. The records are then interpolated to a uniform time step of 0.1 sec (Nyquist frequency of 5 Hz).

FAULT MODEL

The fault parameterization procedure and the method of solving for the distribution of slip are the same as used by Hartzell and Heaton (1983) in their study of the 1979 Imperial Valley earthquake. Faulting is assumed to occur on one planar surface. This surface is subdivided into 192 equal-area subfaults shown in Figure 3. These subfaults are used to construct a number of forward models that give insight

into overall rupture characteristics. Formal inversion procedures are also employed to deduce the distribution of slip on these subfaults that is most compatible with the strong motion data. The inversions are stabilized by requiring that the slip is everywhere positive and by minimizing the difference in dislocation of adjacent subfaults (unless the data strongly requires large differences). Each subfault has a length of 1.0 km and a vertical width of 1.9 km. These subfault dimensions were chosen to accommodate the previously mentioned high-frequency content of the strong motion velocity records. At 1.0 Hz, the S-wave wavelength is approximately 3.2 km and about 1.6 km at 2.0 Hz. The total fault plane extends from a depth of 0.5 km to a depth of 12.0 km and has a length of 32 km. The hypocenter is fixed at a depth of 8.5 km near the northern end of the fault. This value is an average of the depths given by Eaton (1984) and Cockerham and Eaton (1984). Cross-sections of aftershock locations with depth (Cockerham and Eaton, 1984) show an apparent dip that varies from 88°NE on the northern end of the rupture zone to 81°NE on the southern end of the rupture zone. However, with small perturbations to the velocity model, these dips can switch to the southwest (Robert Cockerham, personal communication, 1985). We therefore conclude that the dip of the fault is not resolvably different from 90°. A 90° dip is used for all fault models in this study.

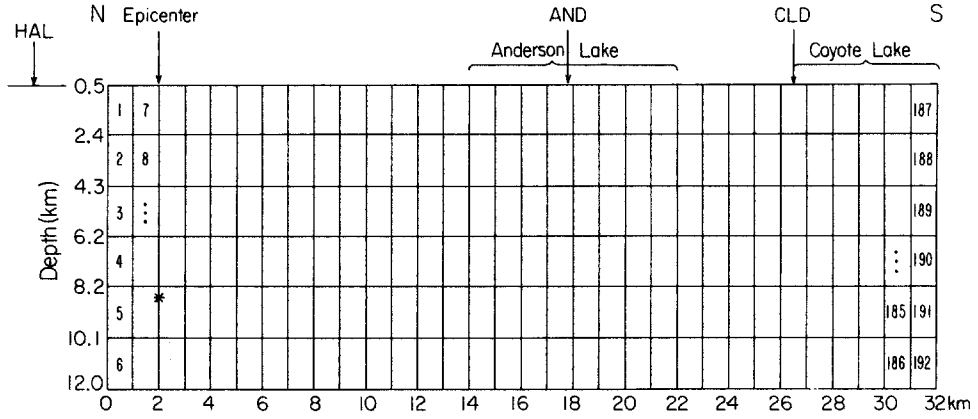

FIG. 3. Side view of parameterized fault showing the 192 subfaults. The hypocenter is indicated by an asterisk.

The strike of the fault plane is fixed at 148° clockwise from north. This value was chosen after considering several estimates of the strike by other investigators: 146° from CALNET first-motion data (Cockerham and Eaton, 1984); 153° from long-period GDSN records (Ekström, 1984); and 144° from long-period IDA records (Hiroo Kanamori, personal communication, 1985). Ekström (1984) found no evidence for resolvable dip-slip motion from a moment tensor inversion of GDSN data. However, the long-period GDSN data gives poor resolution of shallow, dip-slip faulting. But the first-motion fault plane solution and tectonic arguments suggest that any dip-slip motion is secondary to the strike-slip component. We therefore constrain the rake to be 180° and consider only strike-slip mechanisms.

Figure 4 shows the idealized fault plane of Figure 3 in map view, superimposed on the surface expressions of the Calaveras fault system. Two locations are considered for the rupture plane of the Morgan Hill earthquake; model A and model B. These two fault models have the same strike, dip, and depth to the hypocenter, but run parallel to each other. Their respective epicenters are indicated by stars. Model B uses the epicenter of Cockerham and Eaton (1984) and follows their lineation of

aftershock epicenters. Model A is displaced by about 1.5 km to the southwest and follows more closely the surface expression of the Calaveras fault. It has long been recognized that earthquake epicenters along the Calaveras fault and sections of the San Andreas fault in central California tend to locate a few kilometers to the east of the surface trace of the fault (Brown and Lee, 1971; Bolt and Miller, 1971). Mayer-Rosa (1973) attributed the offset of epicenters from the Calaveras fault to a vertical low-velocity zone associated with the fault. More recent studies (Cockerham

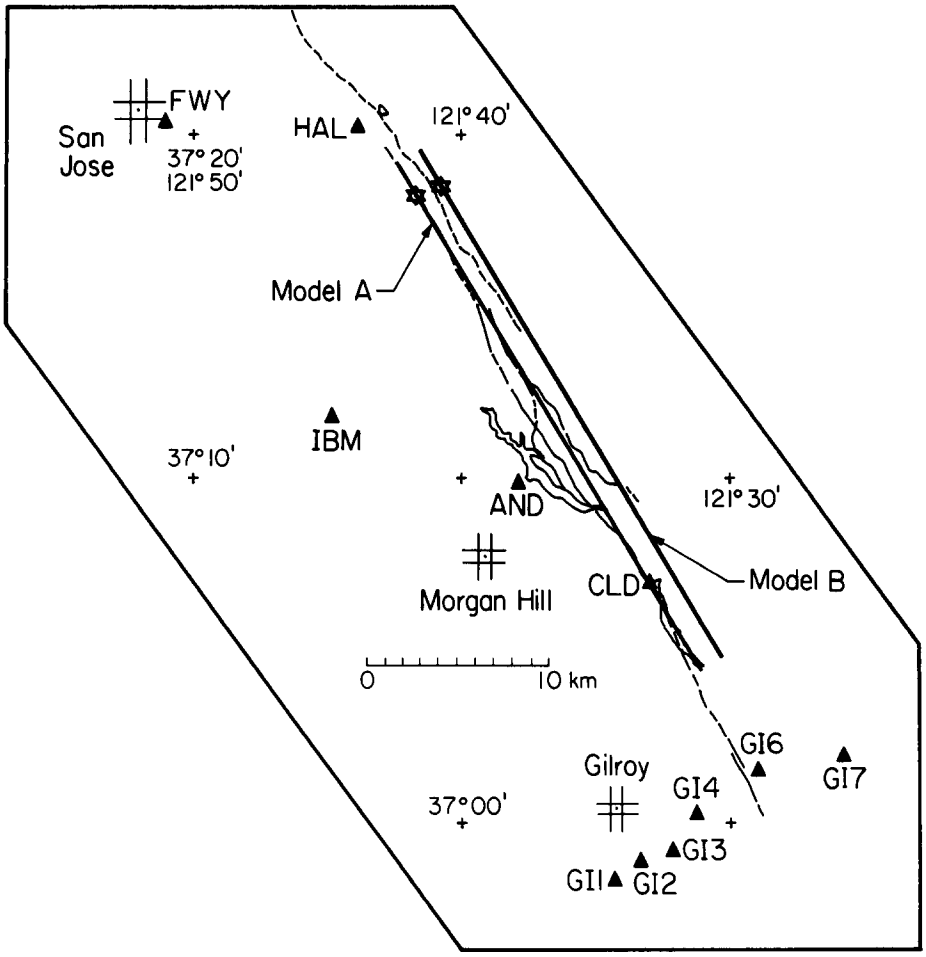

FIG. 4. Map view of the two fault models considered, A and B. Model A more closely follows the surface morphologic expression of the Calaveras fault zone. Model B follows the trend of aftershock locations.

and Eaton, 1984), with absolute location errors of about $\pm\frac{1}{2}$ km, still show the epicenters to the east of the Calaveras fault. Therefore, at this point, it is not clear how much of the offset is real and how much is due to systematic location errors caused by the laterally heterogeneous velocity structure. For this reason, the two fault models A and B are considered. Clearly, more complicated fault models, where the strike and dip vary along the length of the fault, may be more realistic, especially given the complexity of the surface trace of this section of the Calaveras fault. However, we do not consider this more complicated class of models.

Given the above geometry for the fault, an appropriate velocity structure is required for the computation of the crustal response. Fortunately, a considerable

amount of seismic-refraction profiling has been done along the southern Calaveras fault by the U.S. Geological Survey. Blümling *et al.* (1985) present a *P*-wave velocity structure for the area based on this work, and their results are reproduced in Figure 5. For comparison, Figure 5 shows the velocity structure of Ellsworth and Marks (1980) derived for the Livermore section of the Calaveras fault which is located further to the north. The *P*-wave velocity structure we have adopted is given by the

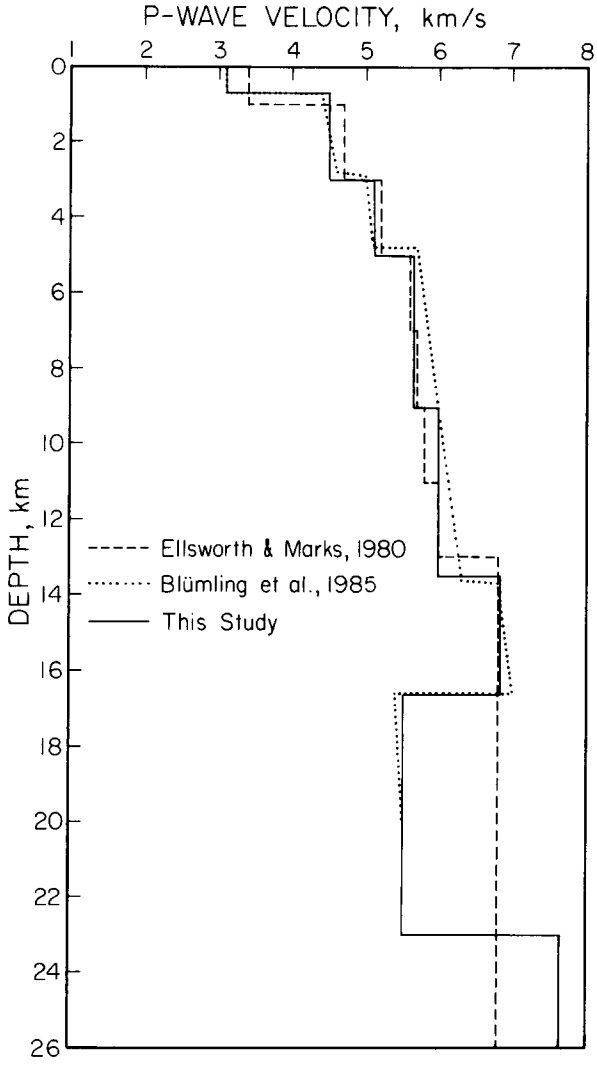

FIG. 5. *P*-wave velocity structures for the Calaveras fault region.

solid line and follows closely the curve of Blümling *et al.* (1985). However, as a computational convenience, the velocity structure used in this study has no velocity gradients, only constant velocity layers. The *S*-wave velocities are obtained from the *P*-wave velocities assuming $\alpha = 2\beta$ in the top layer and $\alpha = \sqrt{3}\beta$ in all other layers. The layer densities are based on empirical data relating *P*-wave velocity and density (Grant and West, 1965). See Table 3 for these values.

The velocity structure we have used in Figure 5 has one clear deficiency; it is a laterally homogeneous model. Seismic-refraction studies indicate that there are

strong velocity contrasts across the Calaveras fault, dipping structures, and a prominent vertical low-velocity zone associated with the Calaveras fault (Mooney and Luetgert, 1982; Mooney and Colburn, 1985; Blümling *et al.*, 1985). The Calaveras low-velocity zone is described by these studies as being about 2 km wide, extending to a depth of several kilometers, and having a *P*-wave velocity of 2.7 km/sec. These complexities are beyond the scope of the present modeling study. However, time delay terms are introduced into the modeling procedure in an attempt to account for the differences in travel times from the assumed laterally homogeneous velocity structure. The determination of these delay terms is discussed in the following section.

TABLE 3

VELOCITY STRUCTURE

Layer	α (km/sec)	β (km/sec)	ρ (gm/cm^3)	H (km)
1	3.1	1.55	2.22	0.7
2	4.5	2.60	2.45	2.3
3	5.1	2.94	2.55	2.0
4	5.65	3.26	2.65	4.0
5	6.0	3.46	2.70	4.5
6	6.8	3.92	2.82	3.1
7	5.5	3.17	2.60	6.4
8	7.6	4.38	2.90	—

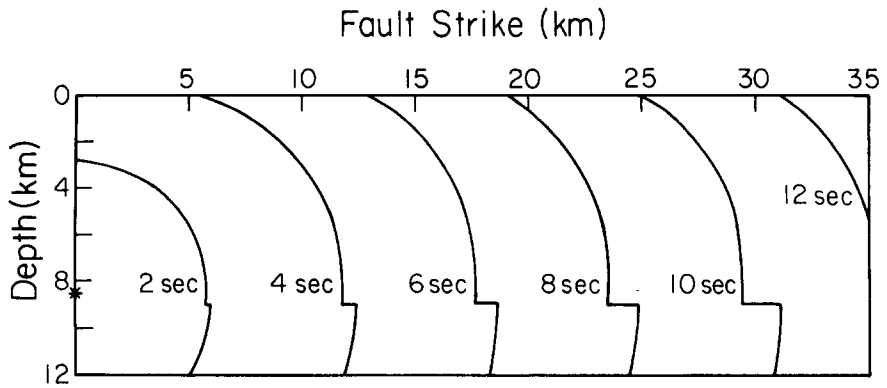

FIG. 6. Snapshots of the position of the rupture front at 2-sec intervals as it advances through the velocity structure of Figure 5 at nine-tenths of the local *S*-wave velocity.

The final information needed to complete our kinematic description of the Morgan Hill earthquake is the time history of the advancement of the rupture over the fault plane. We assume that the rupture velocity is a constant fraction of the local *S*-wave velocity. We further assume that the rupture starts at the hypocenter and spreads outward in a continuous fashion, that is with no discontinuous jumps, until the entire fault plane has slipped. Figure 6 shows snapshots of the position of the rupture front at 2-sec intervals for a rupture velocity of nine-tenths the *S*-wave velocity. Note that in this model, faulting of the lower velocity surface layers lags the deeper part of the fault. The move out of the rupture front at a depth of 9 km is due to the presence of a layer boundary at this depth with a jump in *P*- and *S*-wave velocities. The sharp corners in the rupture front that are introduced by this boundary are undoubtedly physically implausible, and this type of feature produces some high-frequency motions that would not occur given a smooth rupture front.

However, rupture times for individual segments of the fault are always within several tenths of a second of rupture times for a model with a continuous rupture front. If a continuous rupture front was used, the partitioning of slip in the models we show would have been somewhat different. However, these differences are not greater than the model uncertainties introduced by lateral heterogeneities and are thus not resolvable by our analysis. To allow for more flexibility in the kinematic description of the rupture, we introduce the convenience of time windows. Each subfault in Figure 3 slips when the rupture front reaches it. However, slip is allowed to occur on each subfault again during one or two successive time intervals (Olson and Apsel, 1982). These time windows are delayed by a constant amount for all subfaults and represent a constant delay term added to the function plotted in Figure 6. Physically, time windows allow for the possibility of afterslip or faulting that occurs at a lower rupture velocity.

Synthetic ground motions are calculated for each of the strong motion stations in Figure 1 for a fixed dislocation on each of the subfaults of Figure 3. The subfault synthetics are obtained by summing the responses of a large number of closely spaced point sources, delayed to take into account rupture propagation. These point-source responses, or Green's functions, are computed using the generalized reflection-transmission coefficient matrix and discrete wavenumber method of Yao and Harkrider (1983). This technique is useful for calculating higher frequency ground motion (1 to 10 Hz) economically, where precise static displacement values are not important. The subfault synthetics are bandpass-filtered from 0.2 to 5.0 Hz using the same Butterworth filter as applied to the data and convolved with a triangular source-time function with a 0.3-sec duration. This time function was chosen by a trial-and-error fitting process to the data. Figure 7 shows examples of some of the subfault synthetics for fault model A with a strike-slip mechanism and for three components of the data: Halls Valley 240° component; Coyote Lake Dam 285° component, and Anderson Dam 250° component. The three components of observed ground velocity are at the top of the figure. The number at the beginning of each synthetic is the corresponding subfault number. The number at the end of each synthetic is the peak trace amplitude in centimeters/second for a total fault moment of 1.0×10^{26} dyne-cm (i.e., the sum of all the subfaults). This moment is distributed such that the dislocation is the same on each subfault. The timing of the subfault synthetics assumes a rupture velocity of nine-tenths of the local S-wave velocity (i.e., timing in Figure 6). A constrained, damped, least-squares inversion procedure is then used to obtain the best-fitting dislocation for each of the subfaults. The details of this method are given in Hartzell and Heaton (1983).

Modeling Results

Bakun *et al.* (1984) identified a strong source of seismic radiation originating from near Anderson Reservoir based on the timing of S waves on the accelerograms. The same source was noted by Uhrhammer and Darragh (1984) using Berkeley ultra-long-period displacement seismograms. The basis for this interpretation can be seen in Figure 7. The large late pulse on the 240° component of the Halls Valley record lines up with a source near subfaults 99–102, located under Anderson Dam. Waveforms for sources in this area also generally agree with the observed waveforms at the other strong motion stations. The rupture velocity needed to advance the rupture front from the hypocenter to beneath Anderson Reservoir such that synthetic and observed waveforms line up, particularly at Halls Valley, is approximately nine-tenths of the S-wave velocity. This rupture velocity is used for all forward models and for the first time window of all multi-time-window inversion models.

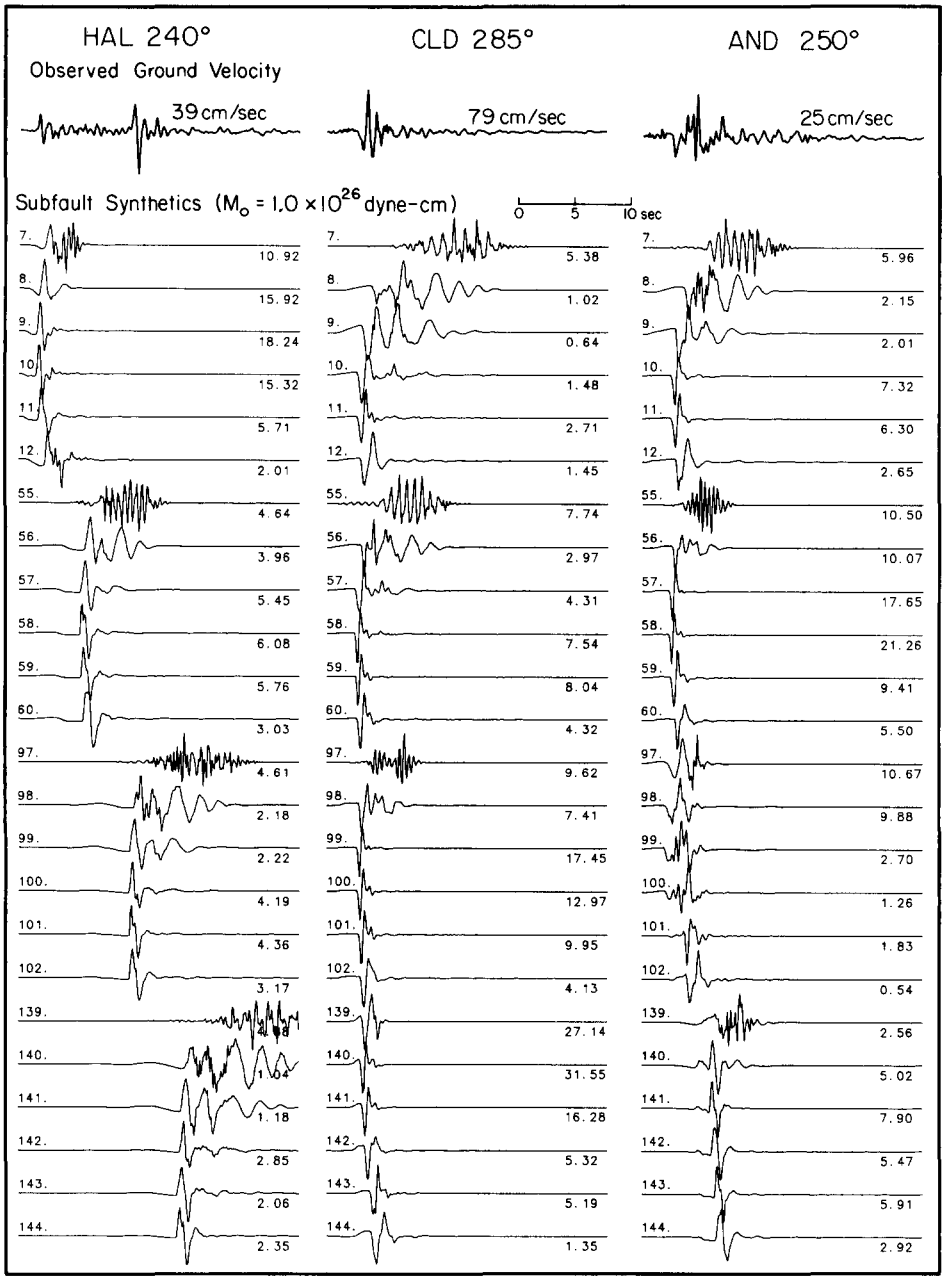

FIG. 7. Synthetic ground velocity records for selected subfaults from the fault parameterization shown in Figure 3. Fault model A in Figure 4 is used with a strike-slip mechanism for the source.

Because of the complexity of some of the data records, as discussed in the data section, a subset of five of the stations in Figure 1 having the cleanest waveforms is used in the modeling. These five stations are: Halls Valley; Coyote Lake Dam; Anderson Dam; Gilroy array station 6; and the IBM station. These stations are also the closest to the rupture.

The final point to clarify before discussing the modeling results is the determination of the station trigger time adjustments. The trigger time is simply the turn-on time of the instrument relative to the origin time of the earthquake. Adjustments to these trigger times are made to account for strong lateral heterogeneities not

present in our velocity model. Table 4 lists the trigger times in seconds after the origin time. The observed values are taken directly from the film records. No timing is available at the IBM station. Trigger times used in the various models are determined as follows. Two different fault models are considered for this purpose; a point-source model, designated F1, and a line source model, designated FL. The point-source model consists of two subfaults; number 10 (at the hypocenter) and number 102 (under Anderson Reservoir) (see Figure 8). The line source model includes all subfaults in the depth interval from 8.2 to 10.1 km from subfault 5 to 119 (see Figure 10). The point-source model and the line source model are considered because they represent end members of a large class of possible solutions. Synthetics are calculated for these two models. The synthetics are then shifted in time until the best correlation is found by eye with the data. This time shift fixes the trigger time. The trigger times obtained by this method are generally within a second of the observed values. Halls Valley has the greatest deviation from the observed value, which is attributed to the ray path being almost entirely within the Calaveras fault low-velocity zone. In fact, the observed trigger time of 3.10 sec at Halls Valley agrees very well with a source at the hypocenter and a P-wave velocity of 2.7 km/

TABLE 4

STATION TRIGGER TIMES FOR FORWARD AND INVERSION MODELING RUNS

Run	Point/Line*	Fault Model	HAL	CLD	AND	GIG	IBM
Observed	—	—	3.10	5.60	4.35	7.70	—
Figure 7	P	A	1.87	6.39	4.13	—	—
F1	P	A	1.87	6.39	4.13	7.48	7.48
FL	L	B	2.11	5.80	3.34	7.28	3.54
30	L	A	1.87	5.90	3.15	7.48	3.25
24	P	B	2.11	6.39	4.13	7.67	7.87
28	L	B	2.11	5.80	3.34	7.28	3.54

* Timing based on point-source model or line source model.

sec, the same velocity obtained from refraction studies mentioned above. Our velocity model is faster, thus the smaller trigger time. The large difference between the trigger times for the point source model, F1, and the line source model, FL, at station IBM is due to the approximately 4 sec required for the rupture front to move from the hypocenter to beneath Anderson Reservoir. At other stations, the timing difference is smaller due to directivity.

The fault models we discuss are arranged in order of increasing complexity. We first consider the two forward models mentioned above, F1 and FL. Three different inversion runs are then discussed, two of which have two time windows and a third with three time windows. The two-point source model, F1, in Figure 8 is a natural first choice to explain the two pulses on the 240° component of Halls Valley. The synthetic velocities for this model are compared with the data in Figure 9. In each case, the data are the upper traces. Peak amplitudes are given in centimeters/ second. The ratio of the moments of the two sources (1 to 10) was obtained by matching the relative amplitudes of the two Halls Valley arrivals. Since this estimate is a one-station determination, the ratio of 1 to 10 is not considered to be as accurate as the ones given below, which are based on teleseismic body waves and inversions of a five-station strong motion data set. Also, this estimate does not account for suspected amplification at the Halls Valley site by the wedge of low-velocity material along the fault zone. The total moment of the earthquake is estimated by minimizing the differences in peak amplitudes between data and synthetics at all the stations.

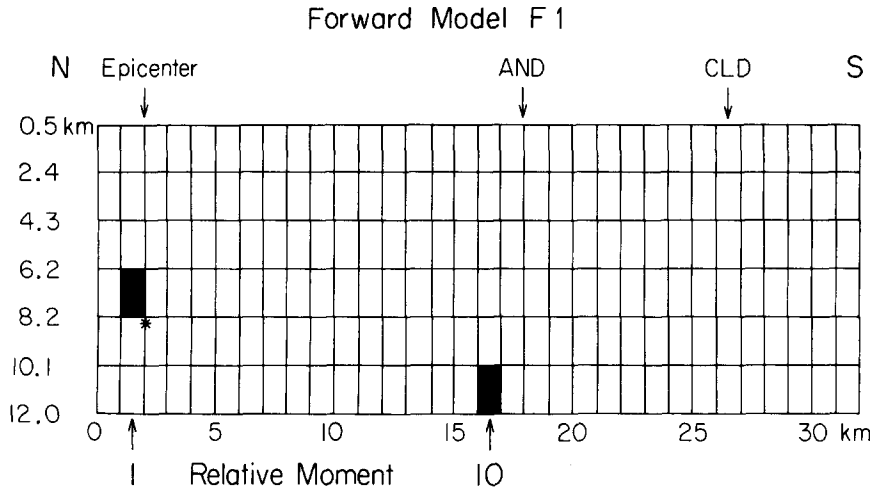

FIG. 8. Simple two-point source forward model consisting of two subfaults with a moment ratio of 10 to 1. The hypocenter is indicated by an asterisk.

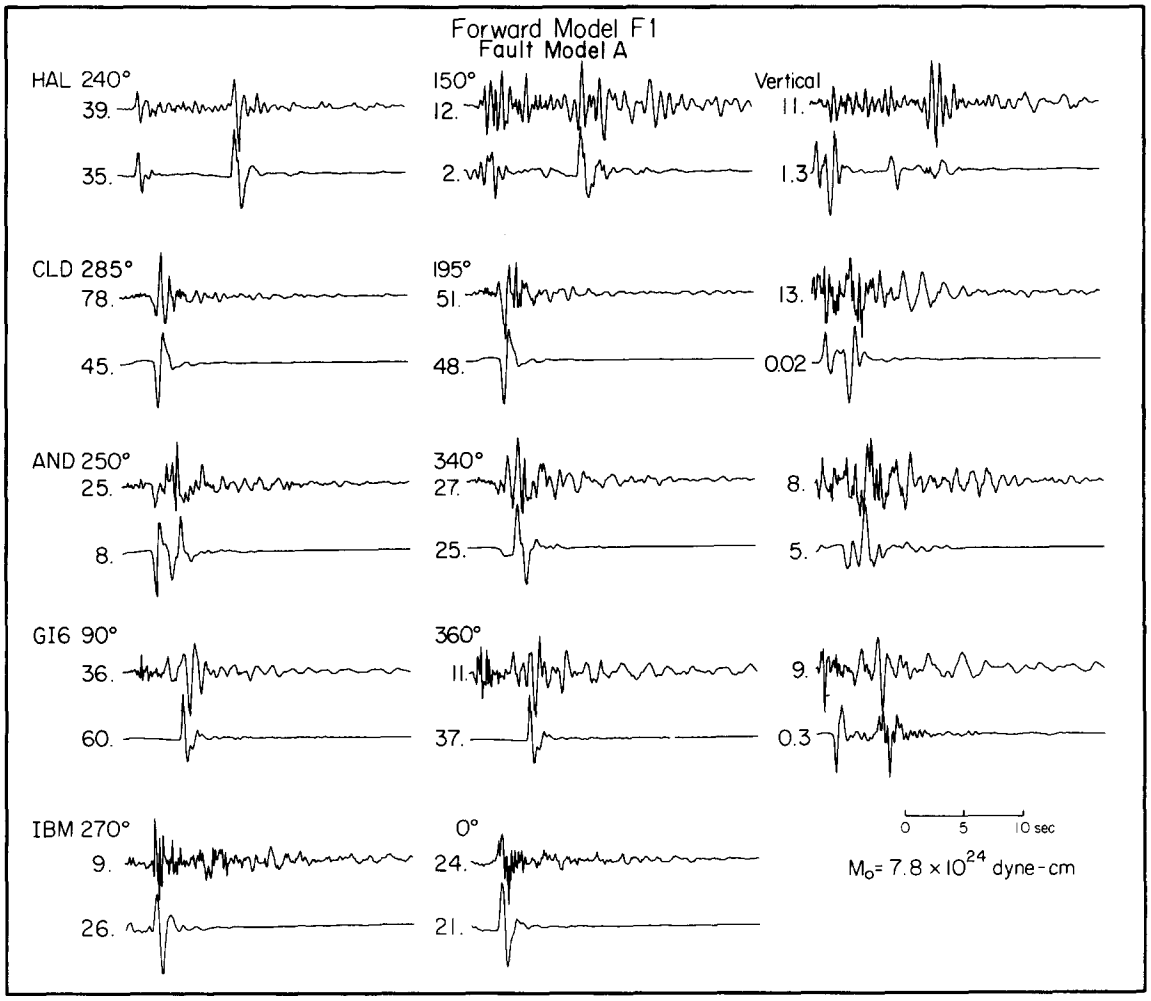

FIG. 9. Comparison of velocity synthetics with the data for point source forward model F1 in Figure 8. The data is the *top trace* of each pair of records. Peak velocities are given in centimeters/second.

Table 6 lists the moment estimates for all of the models. The two-point source model matches the 240° component of the Halls Valley record better than any other model that we present. The 150° and vertical components at Halls Valley have complex waveforms which are not explained by this model or any other model in

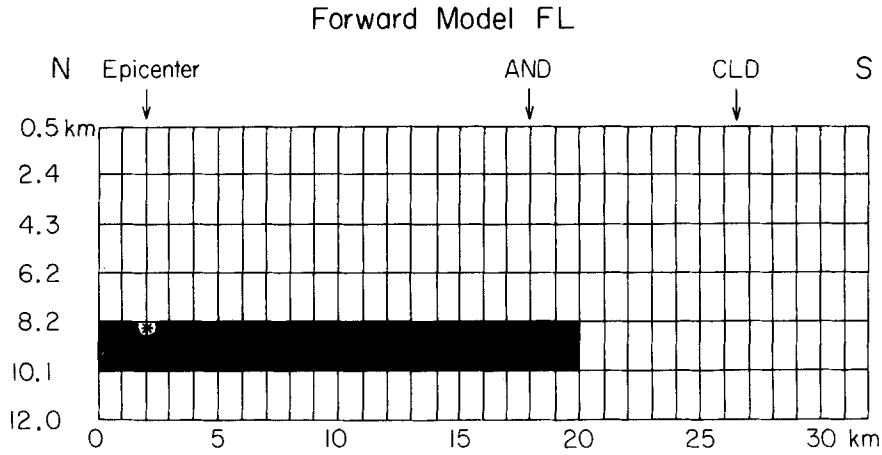

FIG. 10. Simple line source forward model with uniform moment release along its length. The hypocenter is indicated by an asterisk.

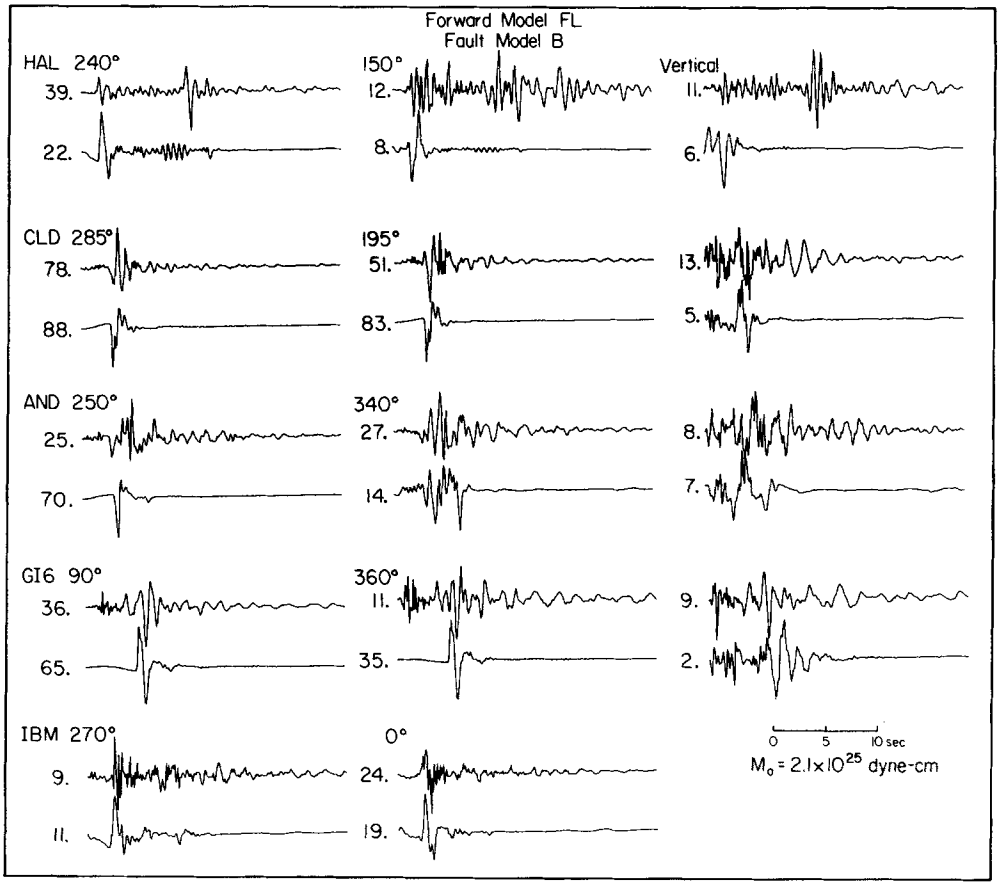

FIG. 11. Comparison of velocity synthetics with the data for line source forward model FL in Figure 10. The data is the *top trace* of each pair of records. Peak velocities are given in centimeters/second.

Table 4. The vertical and 150° components of Halls Valley are near a *P*-wave radiation node and are consequently dominated by scattered energy, which is not accounted for in our simple models. At the other stations, the two-point source synthetics explain some of the major arrivals, but in general, there are many more arrivals in the data.

The line source model of Figure 10 has uniform moment distribution along its length. The synthetics are shown in Figure 11. This model does not explain the two

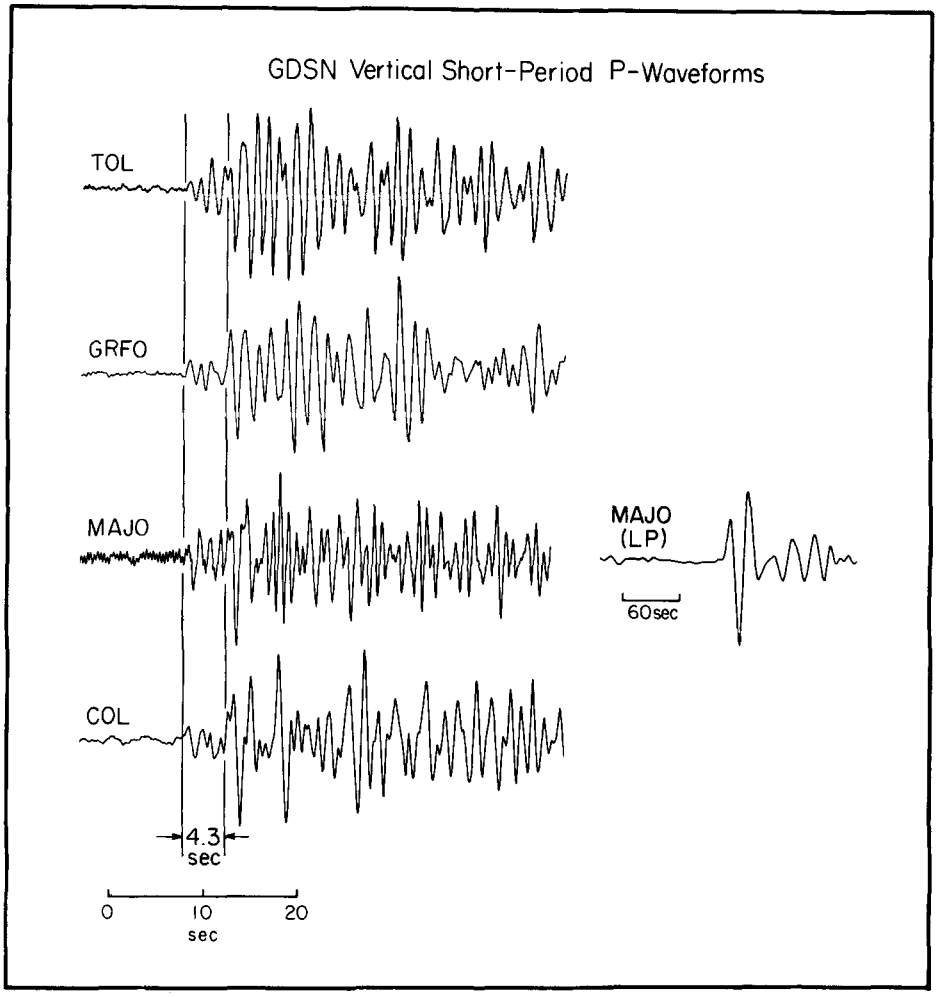

FIG. 12. Teleseismic, short-period, vertical *P*-wave records from GDSN stations for the Morgan Hill earthquake.

arrivals at Halls Valley, but the overall fit to the data is not obviously worse than the two-point source model. However, additional support for a two source model is obtained from short-period, teleseismic body waves. Figure 12 shows GDSN short-period, vertical *P* waves for the Morgan Hill earthquake. The waveforms are characterized by an initial low-amplitude arrival, followed about 4.3 sec later by a much larger phase. This timing is the same as obtained from the local strong motion records for the time difference between the two inferred sources. The one long-period, P-wave record in Figure 12 shows that none of these source details are resolvable on a typical long-period, world-wide recording. Figure 13 shows GRFO

synthetics for several different distributions of faulting. The mechanism is the same in each case; vertical strike-slip fault with a strike of 148° clockwise from north. Synthetics for the other GDSN stations in Figure 12 are very similar and are not pictured. From the top of Figure 13 to the bottom, the five models presented are: (1) single point source at a depth of 8 km; (2) uniform line source at a depth of 8 km; (3) two-point source model with second source three times larger than the first;

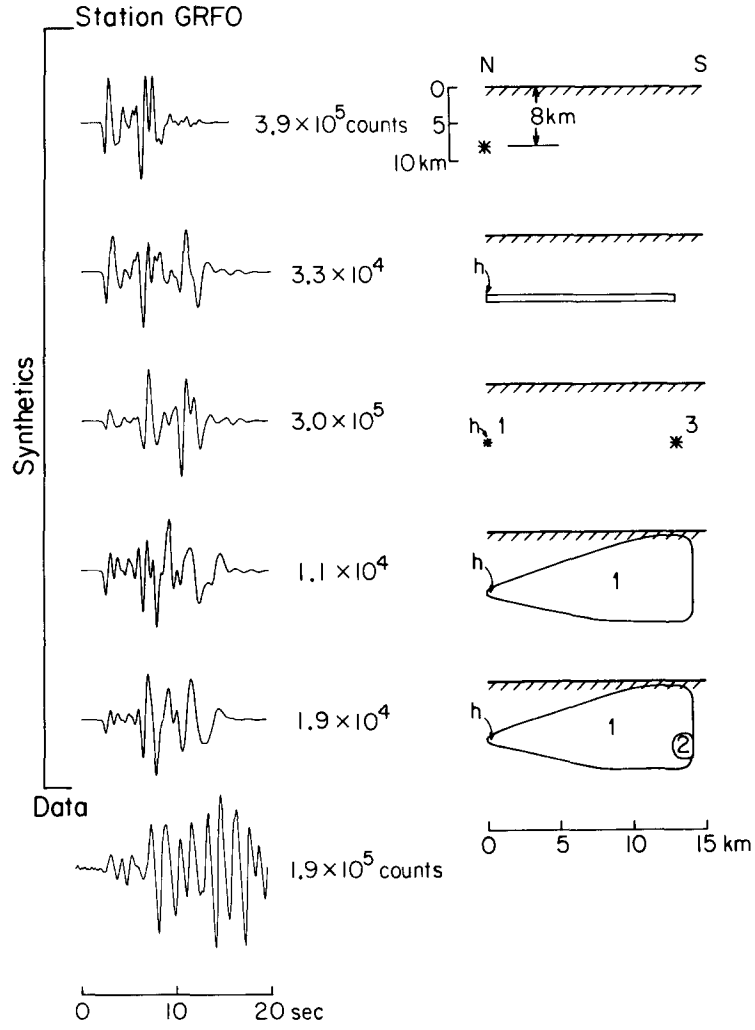

FIG. 13. Short-period, *P*-wave synthetics for SRO station GRFO. The fault models considered are: (1) single point source at a depth of 8 km; (2) uniform line source at a depth of 8 km; (3) two-point source model with second source three times larger than the first; (4) wedge-shaped uniform fault model; and (5) wedge-shaped fault model with patch of two times larger dislocation. Amplitudes in counts for the synthetics are for a moment of 2.0×10^{25} dyne-cm.

(4) wedge-shaped uniform fault model; and (5) wedge-shaped fault model with patch of two times larger slip. The symbol h indicates the hypocenter, and the rupture velocity is a constant 3.25 km/sec for all cases. The single point source and the line source models clearly do not fit the data. The remaining three models are constructed to test the degree to which the moment is uniformly distributed in a two-dimensional wedge-like source or alternatively concentrated in two localized sources. The model which fits the observed waveforms best is the wedge model with a patch

of larger slip. However, this model yields moments of 10^{26} dyne-cm (Table 5), a factor of 5 to 10 greater than the moment estimated from long-period surface waves discussed below (station MAJO is nodal and gives a lower estimate). Moments of this size are unacceptable and are the result of distributing the slip over too large an area. However, the moment estimates obtained from the two-point source model (Table 5) are in better agreement with the long-period moment, although the estimate from station COL is low. The somewhat degraded fit to the waveform produced by this model might be attributed to the lack of scattering in the synthetics, which can cause the data to have a more complicated oscillatory character.

The short-period, teleseismic P waves therefore serve as an important constraint on the gross distribution of slip. The moment must be concentrated in two fairly localized source regions, with a moment partitioning of about 3 to 1. However, to resolve any finer details, one must turn to the strong motion data, and more specifically a formal inversion scheme. As we saw above from models F1 and FL, the waveform and timing details, which one must be concerned with, make forward modeling techniques extremely tedious. The relative weighting of the two source regions of about 3 to 1 is supported by the distribution of slip obtained from the inversion models discussed below. The ultra-long-period displacement seismogram recorded at Berkeley (Uhrhammer and Darragh, 1984) suggests the second source is about 5 times larger than the first. But care must be exercised in interpreting

TABLE 5

MOMENT ESTIMATES FOR GDSN SHORT-PERIOD P WAVES

Station	Type	M_0 Wedge Model (Case 5)	M_0 Two-Point Source Model (Case 3)
TOL	DWWSSN	4.1×10^{26}	2.4×10^{25}
COL	DWWSN	1.0×10^{26}	6.3×10^{24}
GRFO	SRO	2.0×10^{26}	1.3×10^{25}
MAJO	MAJO	1.2×10^{25}	8.8×10^{23}

this record since Berkeley lies near a P-wave radiation node. The weighting of 10 to 1 obtained by the forward model F1 from the amplitudes of the two pulses at Halls Valley is unsubstantiated by the other data.

Contours of strike-slip dislocation in centimeters are plotted for each of the inversion models 24, 28, and 30 in Figures 14 through 16, respectively. Models 24 and 28 contain two time windows separated by 0.3 sec. Model 30 has three time windows, each separated by 0.2 sec and is our preferred solution. We show models 24 and 28 to demonstrate some of the variability produced by the inversion when using different assumptions of fault location and timing. The contours of dislocation for the three different inversions vary in detail from one another, but one common aspect is the existence of two main source regions, one in the north near the hypocenter and a second larger one under Anderson Reservoir.

There is little difference between models 28 and 30 (Figures 14 and 16). These two inversions use the same criterion for selecting the trigger times (Table 4), but different fault models, A and B (Figure 4), are assumed. The synthetics for model 30 are compared with the data in Figure 17. The synthetics for model 28 are very similar. The amplitude of the vertical components at Coyote Lake Dam and Gilroy array 6 are much too small for model 30 because they lie on a P-wave radiation pattern node. Model 28 corrects these amplitudes by moving the fault off-strike from these two stations. However, the same effect could be accomplished by a fault

surface with variable strike or by refraction of waves out of a low-velocity zone along the fault. Of these two, run 30 and fault model A are marginally preferred.

Model 24 (Figure 15) should be compared with model 28 (Figure 14). Both use fault model B. However, model 24 uses the point-source trigger times, and model 28 uses the line source trigger times. Refer to Table 4 and the previous discussion of trigger times. The distribution of dislocation for model 24 (Figure 15) is somewhat more complex. Of these two inversions, model 28 is preferred based on a slightly better fit to the data. However, given the uncertainties in timing, no strong argument can be made for one model over the other. For this reason, the differences between Figures 14 and 15 are an indication of the resolution of the modeling process.

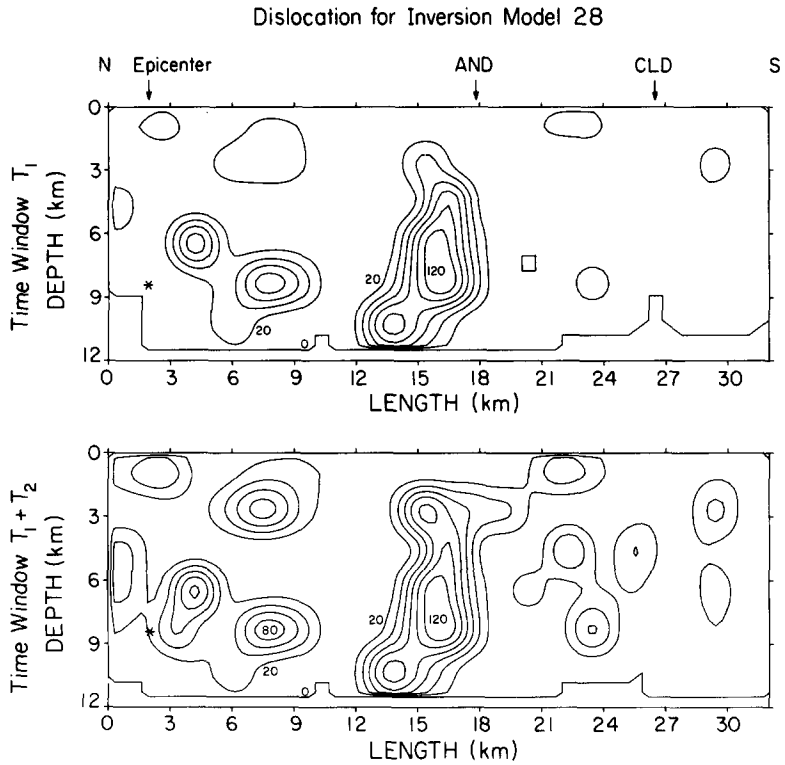

FIG. 14. Contours of strike-slip dislocation in centimeters for inversion run 28 and fault model B. Each frame shows the cumulative dislocation in time windows separated by 0.3 sec. The hypocenter is indicated by an asterisk.

Although models 24 and 28 contain two time windows and model 30 contains three time windows, each still has very limited flexibility in terms of when slip may occur on a given subfault. This condition exists because the two time windows are separated by only 0.3 sec for models 24 and 28, and 0.2 sec for model 30. These small separations are used because the duration of the source-time function for each time window is 0.3 sec, and continuity of the slip history requires this spacing or less for the time windows. Another constraint is the computer time required to solve the least-squares problem for the subfault dislocations. It would be simple to set up a problem with 10 time windows, which would yield the kind of flexibility needed to encompass most plausible fault rupture scenarios. However, computation time increases dramatically as the number of time windows is increased, and such a run would be prohibitive on a VAX 750. But even with these limitations, model 30 does

a fairly good job of explaining most of the major phases in the observed waveforms. This result indicates that the rupture propagated at close to the shear wave velocity with little afterslip. Indeed, we see from Figure 16 that the maximum slip under Anderson Reservoir is reached within the first time window, which occurs at nine-tenths of the local shear wave velocity. Slip in the hypocentral region, however, does continue to grow after the initial passage of the rupture front. Another observation that can be made from Figure 16 is the increase in dislocation with time on the shallower portions of the fault, above 5 km. This progression of faulting is most likely due to the slower rupture velocity in the lower velocity, near-surface sediments (refer to Figure 6).

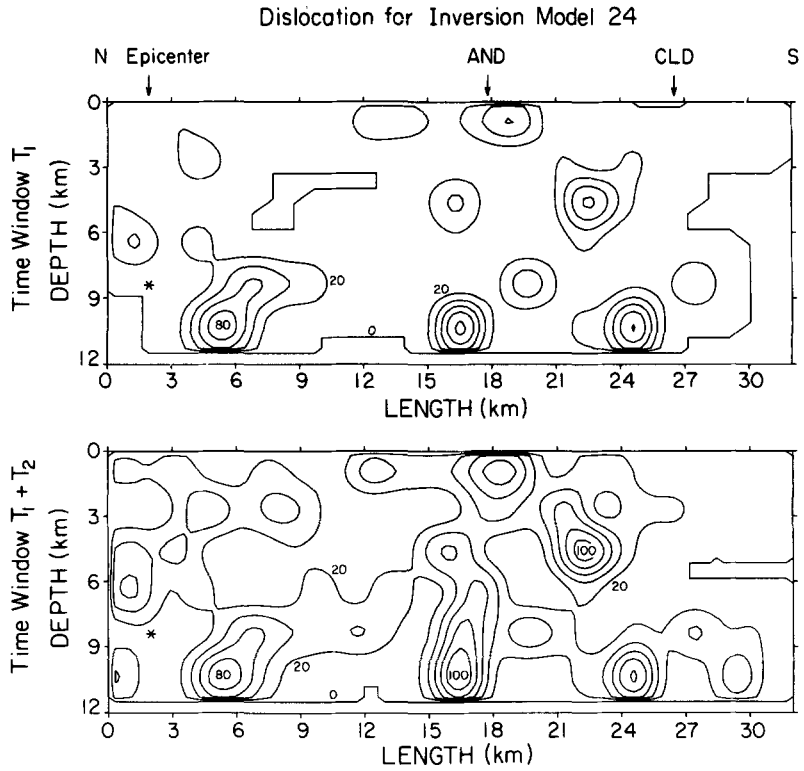

FIG. 15. Contours of strike-slip dislocation in centimeters for inversion run 24 and fault model B. Each frame shows the cumulative dislocation in time windows separated by 0.3 sec. The hypocenter is indicated by an asterisk.

Figure 18 compares the final dislocation for our preferred model 30 with the aftershock distribution of Cockerham and Eaton (1984). The shaded portion of the figure indicates the region of the fault plane which did not experience aftershocks. There is the suggestion from Figure 18 that aftershocks occurred where slip during the main shock did not occur. A similar result is obtained by Doser and Kanamori (1986) for the 1979 Imperial Valley earthquake, when they compare the distribution of slip obtained by Hartzell and Heaton (1983) with their relocated aftershocks.

The moment estimates in Table 6, which are based on modeling of the strong motion records, can be compared with the following estimates from other data: 1.1×10^{25} dyne-cm from broadband displacement seismograms recorded at Berkeley (Uhrhammer and Darragh, 1984); 2.0×10^{25} dyne-cm from GDSN long-period body waves (Ekström, 1984); and 2.3×10^{25} dyne-cm from IDA R1 and R2 phases (Hiroo

Kanamori, personal communication, 1985). The moment of 2.1×10^{25} dyne-cm obtained from model 30 is in good agreement with the above estimates. The other estimates in Table 4 are similar except for run F1. Run F1 (two subfaults only) is probably not the best model to use to estimate the moment because it is too idealized

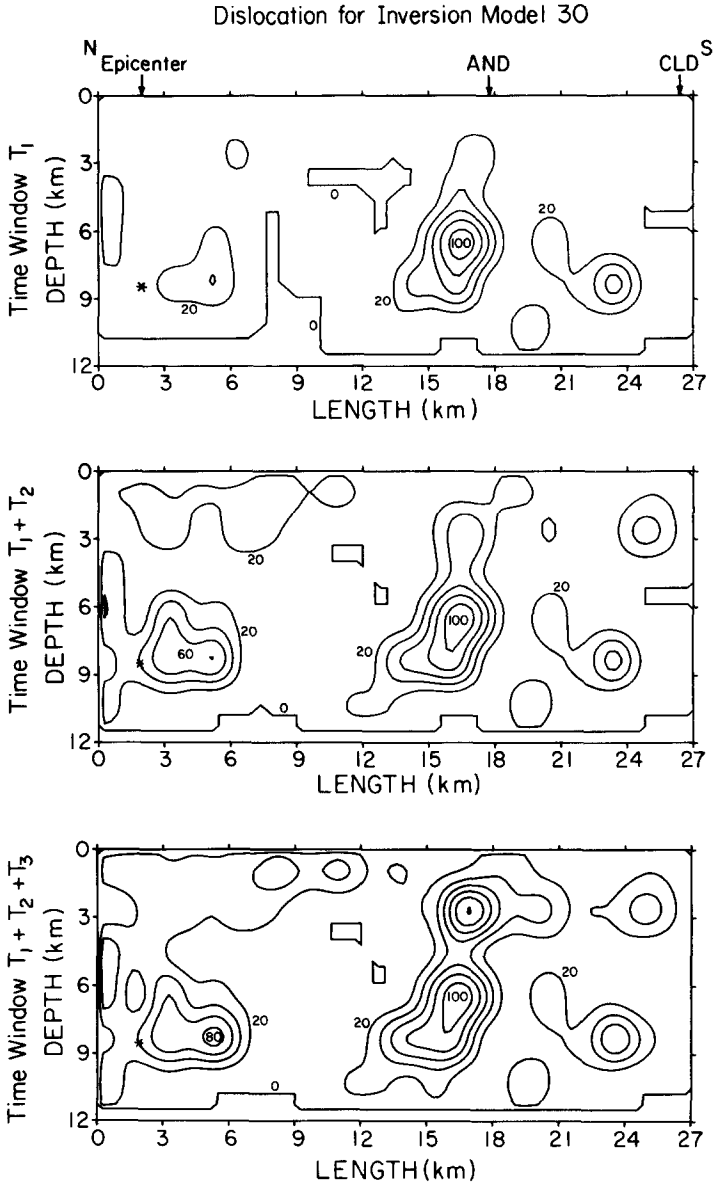

FIG. 16. Contours of strike-slip dislocation in centimeters for the preferred inversion run 30 and fault model A. Each frame shows the cumulative dislocation in time windows separated by 0.2 sec. The hypocenter is indicated by an asterisk.

and simplistic. The column labeled "fit" in Table 6 is the Euclidean norm of the final residual vector. This number is the square root of the sum of squares of the vector components. The smaller this number, the more closely the synthetics match the data. The lower number for model 28 is due to the fact that fewer of the vertical components are near *P*-wave radiation nodes for fault model B.

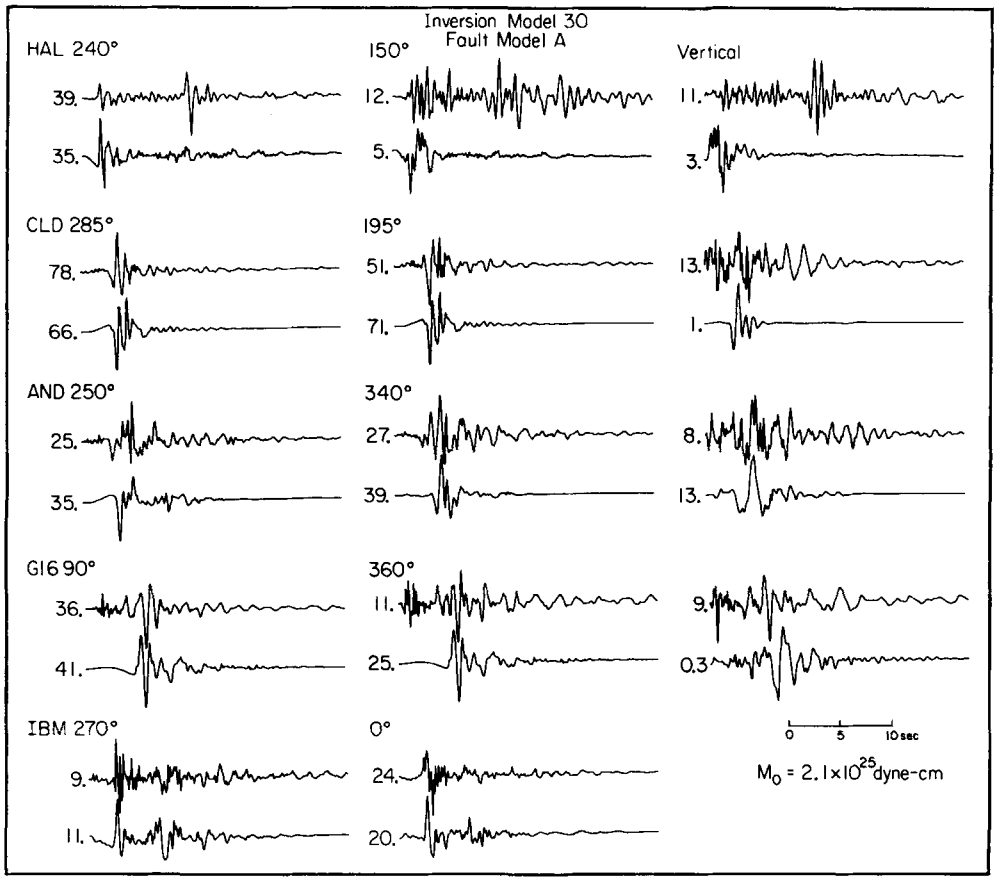

FIG. 17. Comparison of velocity synthetics with the data for inversion run 30. The data is the *top trace* of each pair of records. Peak velocities are given in centimeters/second.

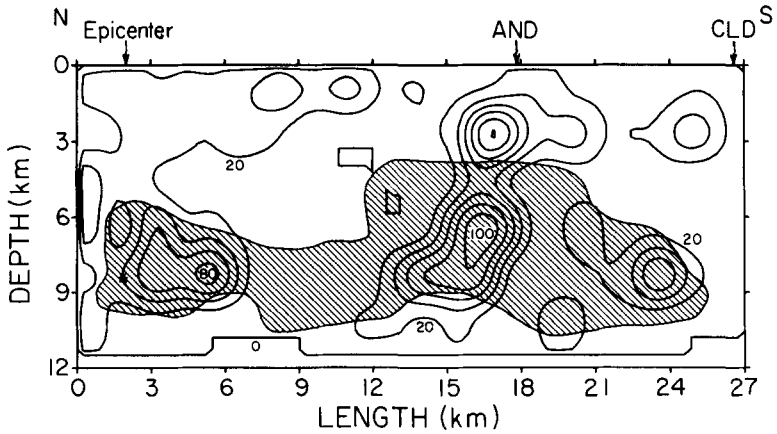

FIG. 18. Comparison of aftershock pattern of Cockerham and Eaton (1984) with final dislocation distribution for the preferred inversion run 30. Aftershocks occurred outside of the *shaded portion* of the fault.

TABLE 6
MOMENT ESTIMATES AND FIT TO DATA

Run	Fault Model	M_0 ($\times 10^{25}$ dyne-cm)	Fit*
F1	A	0.8	—
FL	B	2.1	—
30	A	2.1	9.58
24	B	2.6	9.58
28	B	2.4	9.47

* $\| b - Ax \|$ where $Ax \cong b$.

CONCLUSIONS

The Morgan Hill earthquake is almost entirely a unilateral rupture originating at a depth of about 8.5 km near Halls Valley and propagating to the southeast along the Calaveras fault. Significant slip is terminated near the Coyote Lake Dam station at the northern end of Coyote Lake. The average rupture velocity is approximately nine-tenths of the local shear wave velocity. To first approximation, the Morgan Hill rupture consists of two main source regions separated by about 4.3 sec, one in the north near the hypocenter and a second larger source located under Anderson Reservoir. The idealized, uniform rupture with a "starting-phase" and a "stopping phase" is rejected. The source region under Anderson Reservoir is approximately 3 times larger in moment than the initial source, with a maximum dislocation of about 1 m. On a finer scale, both of these source regions have structure of their own and should not be viewed as two simple point sources. Resolution of this fine structure is hindered by a complex velocity structure with strong lateral heterogeneity. The surface expression of the Calaveras fault zone is very complex in the region of Anderson Reservoir, with many small bifurcated faults. This complexity may be a manifestation of an asperity at depth, which apparently broke during the Morgan Hill earthquake, but which hampers the formation of a simple throughgoing fault. The total amount is estimated from the inversion of the strong motion data to be 2.1×10^{25} dyne-cm.

Bufe *et al.* (1979) and Toppozada (1984) conclude that the same section of the Calaveras fault that ruptured during the Morgan Hill earthquake last broke in 1911, 73 yr earlier. One conceptual model for long-term behavior of this fault is that most of the fault fails through aseismic creep with a few isolated patches (asperities) that lock and store elastic energy. If the asperity that apparently broke in 1984 also broke in 1911, then our estimated maximum dislocation of 1 m would imply an average fault slip rate of 13.7 mm/yr. Savage *et al.* (1979) and Prescott *et al.* (1981) obtained slip rates from geodetic measurements of 17.0 and 8.5 mm/yr for the Calaveras fault south and north of its bifurcation with the Hayward fault, respectively. The Morgan Hill earthquake occurred in the transitional bifurcation region. The estimate of 13.7 mm/yr is very consistent with the geodetic measurements.

ACKNOWLEDGMENTS

The authors thank Homer Givin of IBM Corporation and Robert Nigbor of Kinemetrics for supplying the strong motion record from the IBM Santa Teresa free-field site. The manuscript was significantly improved by thoughtful reviews from Paul Spudich and William Joyner. Carol Horn typed the manuscript.

REFERENCES

Bakun, W. H. (1980). Seismic activity on the southern Calaveras fault in central California, *Bull. Seism. Soc. Am.* **70**, 1181–1197.

Bakun, W. H., M. M. Clark, R. S. Cockerham, W. L. Ellsworth, A. G. Lindh, W. H. Prescott, A. F.

Shakal, and P. Spudich (1984). The 1984 Morgan Hill, California, earthquake, *Science* **225,** 288–291.

Blümling, P., W. D. Mooney, and W. H. K. Lee (1985). Crustal structure of the southern Calaveras fault zone, central California, from seismic refraction investigations, *Bull. Seism. Soc. Am.* **75,** 193–209.

Bolt, B. A. and R. A. Miller (1971). Seismicity of northern and central California, 1965–1969, *Bull. Seism. Soc. Am.* **61,** 1831–1847.

Brady, A. G., R. L. Porcella, G. N. Bycroft, E. C. Etheredge, P. N. Mark, B. Silverstein, and A. F. Shakal (1984). The Morgan Hill, California earthquake of April 24, 1984, *Open-File Rept. 84-498 B* (compiled by Seena Hoose).

Brown, R. D., Jr. and W. H. K. Lee (1971). Active faults and preliminary earthquake epicenters (1969–1970) in the southern part of the San Francisco Bay region, U.S. Geol. Survey Map MF-307.

Bufe, C. G., W. H. Bakun, and T. V. McEvilly (1979). Historic seismic activity and the 1979 Coyote Lake sequence, *EOS* **60,** 891.

Cockerham, R. S. and J. P. Eaton (1984). The April 24, 1984 Morgan Hill earthquake and its aftershocks: April 24 through September 30, 1984, in *The 1984 Morgan Hill, California Earthquake*, CDMG Special Publication 68.

Cormier, V. F. and P. Spudich (1984). Amplification of ground motion and waveform complexity in fault zones: examples from the San Andreas and Calaveras faults, *Geophys. J. R. Astr. Soc.* **79,** 135–152.

Doser, D. and H. Kanamori (1986). Depth of seismicity in the Imperial Valley region (1977–1983) and its relationship to heatflow, crustal structure, and the October 15, 1979 earthquake, *J. Geophys. Res.* **91,** 675–688.

Eaton, J. P. (1984). Location, focal mechanism, and magnitude of the Morgan Hill earthquake derived from the CALNET records, *U.S. Geol. Surv., Open-File Rept. 84-498 A*, 10–17.

Ekström, G. (1984). Centroid-moment tensor solution for the April 24, 1984 Morgan Hill, California, earthquake, in *The 1984 Morgan Hill, California Earthquake*, CDMG Special Publication 68.

Ellsworth, W. L. and S. M. Marks (1980). Seismicity of the Livermore Valley, California region, 1969–1979, *U.S. Geol. Surv., Open-File Rept. 80-515.*

Feng, R. and T. V. McEvilly (1983). Interpretation of seismic reflection profiling data for the structure of the San Andreas fault zone, *Bull. Seism. Soc. Am.* **73,** 1701–1720.

Grant, F. S. and G. F. West (1965). *Interpretation Theory in Applied Geophysics*, McGraw-Hill, New York.

Hartzell, S. H. and T. H. Heaton (1983). Inversion of strong grund motion and teleseismic waveform data for the fault rupture history of the 1979 Imperial Valley, California, earthquake, *Bull. Seism. Soc. Am.* **73,** 1553–1583.

Mayer-Rosa, D. (1973). Travel-time anomalies and distribution of earthquakes along the Calaveras fault zone, California, *Bull. Seism. Soc. Am.* **63,** 713–729.

Mooney, W. D. and J. H. Luetgert (1982). A seismic refraction study of the Santa Clara Valley and southern Santa Cruz Mountains, west-central California, *Bull. Seism. Soc. Am.* **72,** 901–909.

Mooney, W. D. and R. H. Colburn (1985). A seismic-refraction profile across the San Andreas, Sargent, and Calaveras faults, west-central California, *Bull. Seism. Soc. Am.* **75,** 175–191.

Niazi, M. (1984). Radial asymmetry of the observed PGA and question of focusing in the near-source region of April 24, 1984 Morgan Hill earthquake, in *The 1984 Morgan Hill, California Earthquake*, CDMG Special Publication 68.

Olson, A. H. and R. J. Apsel (1982). Finite faults and inverse theory with application to the 1979 Imperial Valley earthquake, *Bull. Seism. Soc. Am.* **72,** 1969–2001.

Oppenheim, A. and R. Schafer (1975). *Digital Signal Processing*, Prentice-Hall, Englewood Cliffs, New Jersey.

Prescott, W. H., M. Lisowski, and J. C. Savage (1981). Geodetic measurements of crustal deformation on the San Andreas, Hayward, and Calaveras faults near San Francisco, California, *J. Geophys. Res.* **87,** 10637–10655.

Savage, J. C., W. H. Prescott, M. Lisowski, and N. King (1979). Geodolite measurements of deformation near Hollister, California, 1971–1978, *J. Geophys. Res.* **84,** 7599–7615.

Shakal, A. F., R. W. Sherburne, and D. L. Parke (1984). CDMG strong-motion records from the Morgan Hill, California earthquake of 24 April 1984, OSMS Report 84-7.

Switzer, J., D. Johnson, R. Maley, and R. Matthiesen (1981). Western hemisphere strong-motion accelerograph station list, *U.S. Geol. Surv., Open-File Rept. 81-664.*

Toppozada, T. R. (1984). History of earthquake damage in Santa Clara County and comparison of 1911 and 1984 earthquakes, in *The 1984 Morgan Hill, California Earthquake*, CDMG Special Publication 68.

Uhrhammer, R. A., and R. B. Darragh (1984). The 1984 Halls Valley (Morgan Hill) earthquake sequence:

April 24 through June 30, in *The 1984 Morgan Hill, California Earthquake*, CDMG Special Publication 68.

Yao, Z. X. and G. G. Harkrider (1983). A generalized reflection-transmission coefficient matrix and discrete wavenumber method for synthetic seismograms, *Bull. Seism. Soc. Am.* **73**, 1685–1699.

U.S. GEOLOGICAL SURVEY
CALIFORNIA INSTITUTE OF TECHNOLOGY
PASADENA, CALIFORNIA 91125

Manuscript received 25 October 1985